Path-integral Monte Carlo study of a model adsorbate with internal quantum states

D. Marx, P. Nielaba, and K. Binder
Institut für Physik, Universität Mainz, Staudinger Weg 7, D-6500 Mainz, Federal Republic of Germany
(Received 20 August 1992)

An adsorbate in the strong-binding and small-corrugation limit is studied. The resulting two-dimensional fluid is treated in the adiabatic approximation: the translations of the particles are treated classically, whereas the internal quantum degrees of freedom are modeled by interacting two-state tunneling systems. The temperature-coverage phase diagram is obtained to a high degree of precision by combining finite-size-scaling ideas with path-integral Monte Carlo techniques. Even this simplified adsorbate model possesses a surprisingly complex phase diagram including first- and second-order transitions as well as a tricritical and a triple point. We identify gas, liquid, fluid, and square-lattice solid phases combined with a preferred internal quantum state depending on temperature and coverage. We determine the order of the transitions and localize the different phase boundaries of this many-body quantum system reliably. Mean-field approximations and low-density expansions are compared to the simulations. A possible extension of the block analysis method to determine triple points and solid coexistence densities is discussed.

I. INTRODUCTION AND MOTIVATION

Two-dimensional (2D) layers of molecules adsorbed on surfaces have become an active field of research[1–6] during the last decade. Experimental[5,6] as well as theoretical[7–9] investigations show the need to take the translations into account quantum mechanically in order to describe light adsorbates appropriately. Another class of molecules having internal degrees of freedom, as, for example, rotational motion[10,11] or magnetic moments,[12,13] calls for a *quantum* treatment of these *internal* coordinates even if the translations can still be treated classically. The first step is to investigate one particle with such an internal quantum degree of freedom coupled to a classical bath of surrounding particles, as, e.g., considered recently in Refs. 14 and 20. A more realistic model consists of a classical fluid where each molecule is supplemented by a two-level system, which in turn is represented as a quantum spin. These models have a long history, as documented in the certainly incomplete list in Refs. 15–18. Some recent work in this direction, i.e., fluids with internal quantum states, and more references to earlier work can be found in Ref. 19. A very challenging aspect of these many-body quantum systems is the calculation of cooperative effects, i.e., equilibrium phase diagrams, based on microscopic knowledge of the corresponding intermolecular potentials only. But such calculations, necessarily using computer simulation methods, have remained of outstanding interest since the introduction of these techniques even for use in classical systems. Despite very impressive progress[21,22] along these lines, it still is a difficult problem (even for a simple classical fluid) to study the region near the critical point of the gas-liquid transition, and to precisely estimate the location of the gas-liquid coexistence curve. Although this problem has been considered extensively and various well-documented approaches exist with which to deal with first-order transitions[23] (see Refs. 24 and 25 for the recently introduced Gibbs method for fluids being successful away from the critical region, and Ref. 26 for a very extensive grand-canonical finite-size study of the critical 2D Lennard-Jones fluid), there still is need for additional and complementary approaches, even in the case of simple classical fluids.

In this paper, we demonstrate that the successful *combination* of well-known path-integral Monte Carlo (PIMC) simulation methods for quantum systems with finite-size-scaling block analysis techniques is a very promising way of calculating involved phase diagrams of *model* systems with internal quantum degrees of freedom to a yet unknown accuracy. The emphasis is to establish reliable methods for dealing with the effects of strong interactions on the internal structure of the admolecules. At the present stage, our model system is fairly simple, but nevertheless computationally demanding. It consists of hard disks, each bearing a quantum Ising spin. The spin interaction is mediated via a distance dependent coupling of the square well type. Notwithstanding the simplicity of the model, the phase diagram of this model adsorbate already includes many challenging features, such as a tricritical and a triple point, various phase coexistences and second-order magnetic transitions in the internal quantum states.[27] We consider the present study as a *prototype example* of a phase diagram calculation of combined classical-quantum systems in 2D, and not as a model designed to describe a given real system as closely as possible.

Now we give a short outline of the structure of the paper. In Sec. II we introduce the model, discuss different facetes of the underlying Hamiltonian, and make connection to real adsorbates. Section III is devoted to the methods used. In Sec. III A we explain the block analysis method as generalized to off-lattice systems and the gas-solid coexistence, we give the details of how to extract the

quantities of interest, and we illuminate the methodological limitations. In Sec. III B, the formulas necessary to set up the PIMC simulation are presented together with technical details of the simulation. This section closes in C with a short digression of the mean-field (MF) theory and the low-density expansions for the Hamiltonian. We present and discuss our results in Sec. IV, where we start in Sec. IV A with the central quantity, the density distribution. The phase diagram is presented in Sec. IV B and Sec. IV C deals with the determination of the special points and the solid phases. A small part of these results has been communicated in a preceding letter.[27] We close in Sec. V with a summary.

II. DESCRIPTION OF THE MODEL

We study a model adsorbate of N molecules on a flat surface, i.e., the surface has the only effect of forcing the molecules to move strictly in 2D without introducing any corrugation effect.[28] Thus we consider the case of an adsorbate in the strong binding but small corrugation limit. Our methods are by no means restricted to this limit: in principle nothing would prevent us from including corrugations via a suitable periodic potential. Including the third dimension perpendicular to the substrate, allowing for accommodation of possibly growing multilayers, would be computationally somewhat more demanding. The relevant internal quantum states, the two-state tunneling systems, are represented as quantum Ising spins with distance dependent couplings. We assume the mass μ of the molecules to be sufficiently large to justify an *adiabatic approximation* and treat the translational degrees of freedom classically. The molecular center of mass can take continuous values in a monolayer of dimension $S \times S$. The resulting combined classical-quantum N-particle Hamiltonian of the system reads

$$\hat{H}^N = \sum_{i=1}^{N} \frac{\mathbf{p}_i^2}{2\mu} - \frac{1}{2}\omega_0 \sum_{i=1}^{N} \hat{\sigma}_i^x + \sum_{i<j} U(r_{ij}) - \sum_{i<j} J(r_{ij})\hat{\sigma}_i^z \hat{\sigma}_j^z, \tag{1}$$

$$\hat{H}^N = K + \hat{V}, \tag{2}$$

where $\mathbf{p}_i$ and $\mathbf{r}_i$ are momentum and position in 2D of particle i ($r_{ij} = |\mathbf{r}_i - \mathbf{r}_j|$), $\hat{\sigma}^x$ and $\hat{\sigma}^z$ are the usual Pauli spin-1/2 matrices. K and $\hat{V}$ represent the kinetic and potential energies, respectively. The potential energy $\hat{V}$ consists of a one-particle (two-level) part $\omega_0/2$ and two pair interaction terms $U(r)$ and $J(r)$, where U is a hard disk potential for particles with diameter R and $J(r) = J$ for $R < r < 1.5\,R$ and zero elsewhere. Concerning the thermodynamic treatment of the translational and spin degrees of freedom, two distinct averaging procedures are possible. In this study we only do *annealed averages*, i.e., the classical positions and internal quantum states are treated on the same footing. For other examples of systems which can be modeled to a greater or lesser extent in this way, see Refs. 15–18. A quenched average can be realized, if the positions of the molecules are kept frozen in a given configuration and the spin degrees evolve in this surrounding; for disordered configurations, a disorder average has to be performed additionally. The special case of an underlying regular pinning of the spins is the genuine model of statistical mechanics of lattice models.

Our two-state molecules have an internal Hamiltonian $-\omega_0\hat{\sigma}^x/2$ and interact via a pair potential depending on their actual internal state, the hard disk part is the only remnant of the core-core interactions of the molecules. The important feature of the Hamiltonian (1) is that the interaction term will tend to lift particles out of their internal ground state, corresponding to a change of their preferred internal state. Due to the distance dependence of the interaction term $J(r)$, the quantum and classical dynamics are nontrivially coupled. Thus a coverage induced change of the preferred internal quantum state of the molecules is expected. For a given density, there are three classical limits possible: the usual high-temperature limit, but also the limits $\omega_0/J \to 0$ and $\omega_0/J \to \infty$, where only commuting operators are left in the Hamiltonian (1). At infinite temperature, only the hard core repulsion remains, similar to the $\omega_0/J \to \infty$ limit, which produces a one-component classical system with only hard disk $U(r)$ interactions. The opposite limit corresponds to a two-component classical system with attractive interactions $J(r)$ between particles of the same species. The ratio ω_0/J can be considered as the *quantum strength parameter* of our problem.[19] We study the Hamiltonian as a function of temperature and number density (coverage) mainly by PIMC methods (see Refs. 29–35 for a general overview) for a tunneling frequency ω_0 fixed to settle the system down in the quantum regime $0 \ll \omega_0/J \ll \infty$.

A real system with similar properties are O_2 monolayers on graphite: O_2 possesses a magnetic moment (our two-level internal quantum state) which couples to the translations.[12,13] Since the relevant transitions occur above 10 K, the O_2 translations (large mass) may be treated in the adiabatic approximation. In addition, these O_2 films have quasi-2D properties[13] and show only incommensurate structures.[13] The only effect the substrate potential has is to confine the particles to 2D without introducing a commensurate superstructure. Thus we consider a *model adsorbate* in the limit of strong physisorption but nevertheless small corrugation and take into account only the predominant admolecule-admolecule interactions. Of course, we do not aim at a realistic model of O_2 monolayers, which would require more complicated potentials and a quantum Heisenberg spin with antiferromagnetic coupling rather than a ferromagnetic Ising spin model in a transverse field. In the present work, we are only attempting to develop the necessary methodology, while the realistic modeling of actual adsorbates is deferred to future work, see Sec. V.

III. METHODOLOGY

A. Density distribution function and its cumulant

We apply the approach of the cumulant method for off-lattice systems[36,37] to a 2D fluid with internal quan-

tum states defined by the partition function (18). Our method is an extension of finite-size-scaling block analysis techniques, which are a standard tool for the analysis of phase transitions[38] of lattice models.[39,40] While for a Monte Carlo simulation in the NVT ensemble of a fluid (N being the particle number, V the total volume of the box, and T the temperature) the average density $\bar{\rho} = N/V$ of the total system is strictly constant, we can observe fluctuations of the density in *subsystems*. For a liquid-gas phase transition, the density difference between the liquid and the gas phases is the *order parameter* of the phase transition, and hence studying density fluctuations is of key importance for the understanding of this phase transition. The change in the properties of the density distribution function of subsystem cells contains fairly complete information on the liquid-gas transition. We shall show that the densities of coexisting phases can be estimated reliably from the density distribution function. We also present here for the first time a discussion of the implications of a systematic study of the density distribution functions for the gas-*solid* transition and the *triple* point. The behavior of the compressibility and the location of the critical point can also be extracted from the information contained in these distribution functions.

While the spirit of our approach is related to the idea underlying the Gibbs-NVT ensemble,[24,25] namely studying phase coexistence between two system cells directly (one cell being in the fluid state, the other in the gas state, and the cells are able to exchange atoms at constant total volume and temperature) the distinguishing feature of our approach is the introduction of finite-size-scaling concepts[41] which thus allow a *systematic* study of size effects.

In the following, we outline the block analysis method suited for the phase diagram of interest in this study. The subdivision of a total system into *cells* or *blocks* of finite dimension L and studying properties on the footing of these blocks is a familiar concept[42,43] in the statistical mechanics of many-body systems. Defining the particle number in the ith block as N_i, with $\sum_i N_i = N$, the density ρ_i in this block becomes

$$\rho_i = \frac{N_i}{L^d},$$

where

$$L = \frac{S}{M_b} \text{ and } M_b \text{ integer}, \tag{3}$$

S being the linear dimension of the total system with volume $V = S^d$; for the sake of generality, we consider here a d-dimensional system. Thus $(S/L)^d = M_b^d$ subsystems are studied simultaneously and improve the statistics. In Fig. 1, we partition the simulation box containing an actual snapshot configuration from a simulation near the tricritical point into 16 subsystems, i.e., $M_b = 4$. In order to visualize the fluctuations in density and internal quantum states, we represent particles with down (up) average magnetic moments by small (large) circles [we define the average magnetic moment of the ith particle as $(1/P)\sum_{p=1}^{P} S_{i,p}$, the total magnetization itself is defined in Sec. III B, but we show only coarse grained average moments in the snapshot pictures, i.e., the ith particle is represented by a small (large) circle if its average magnetic moment is less (larger) than zero]. Note also that we use the same particle configurations to investigate a whole set of different subsystem sizes in one simulation run, and thus the study of a single (but large enough) system already allows some estimation of finite-size effects. Besides, one simulation run in the coexistence region also yields useful information on gas and liquid phases.

We focus attention on the density distribution function $P_L(\rho)$ where $P_L(\rho)$ is defined as the average of the density distributions $P_L(\rho_i)$ for a given length L of the blocks and $i = 1, \ldots, M_b^d$, i.e., all subsystems of the corresponding block size are considered to behave independently and are averaged together. Consequently thermal averages $\langle\ \rangle_L$ are understood to be taken with a given block size L, but we use that subscript only in this subsection. The different moments of P_L,

$$\langle \rho^k \rangle_L = \int \rho^k P_L(\rho) d\rho, \tag{4}$$

are of key importance in the following digression. Note that the zeroth moment is fixed by normalization of the distribution and the first moment $\langle \rho \rangle_L = \bar{\rho} = N/V$ is the same on all length scales since N and V are fixed.

For a state within the one-phase region, the distribution $P_L(\rho)$ is approximately Gaussian if L exceeds by far the correlation length ξ of the order parameter fluctuations (i.e., density fluctuations), $L \gg \xi$,

$$P_L(\rho) \propto \frac{1}{\bar{\rho}(K^{(L)})^{1/2}} \exp\left[-\frac{\beta(\rho - \bar{\rho})^2 L^d}{2\bar{\rho}^2 K^{(L)}}\right] \tag{5}$$

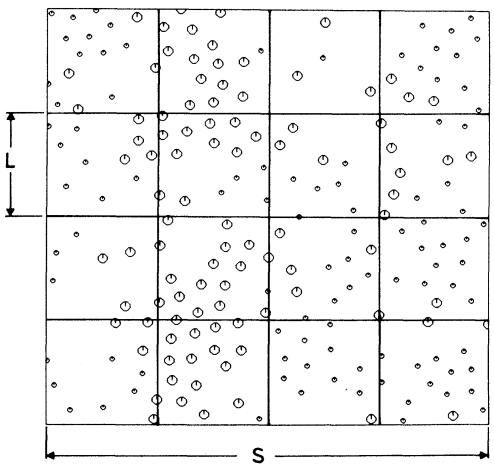

FIG. 1. Blocking of the simulation box containing a configuration near the tricritical point ($N = 200$, $T^* = 0.52$, $\bar{\rho}^* = 0.42$, $\omega_0/J = 4$, $J = 1$, $T^*P \approx 40$). The total system of boxlength S is divided into subsystems of linear dimension $L = S/M_b$; we present the case $M_b = 4$. To visualize in addition to the density fluctuations also the magnetic fluctuations in the internal quantum states, we distinguish particles with different average magnetic moments, see text, with large (up) and small (down) circles.

and it is centered around the density of the overall system $\bar{\rho}$. The second moment of this unimodal Gaussian can be related by standard fluctuation relations to the isothermal compressibility $K^{(L)}$,

$$\langle(\Delta\rho)^2\rangle_L = \langle(\rho-\bar{\rho})^2\rangle_L = L^{-d}\,\bar{\rho}^2\,K^{(L)}/\beta, \tag{6}$$

where $\beta = (k_B T)^{-1}$, and our notation emphasizes that $K^{(L)}$ is the standard isothermal compressibility only in the *thermodynamic limit*, while for small L we expect systematic deviations due to finite-size effects, which shall be discussed later.

The situation is different for a state in a two-phase region where (5) has to be replaced by (again assuming $L \gg \xi$)

$$P_L(\rho) \propto \frac{\rho_{\rm liq}-\bar{\rho}}{\rho_{\rm liq}-\rho_{\rm gas}}\,\frac{1}{\rho_{\rm gas}(K^{(L)}_{\rm gas})^{1/2}}\,\exp\left[-\frac{\beta(\rho-\rho_{\rm gas})^2 L^d}{2\rho^2_{\rm gas}K^{(L)}_{\rm gas}}\right] + \frac{\bar{\rho}-\rho_{\rm gas}}{\rho_{\rm liq}-\rho_{\rm gas}}\,\frac{1}{\rho_{\rm liq}(K^{(L)}_{\rm liq})^{1/2}}\,\exp\left[-\frac{\beta(\rho-\rho_{\rm liq})^2 L^d}{2\rho^2_{\rm liq}K^{(L)}_{\rm liq}}\right], \tag{7}$$

the derivation of which can be found in Ref. 36. In (7), we have approximated a general bimodal distribution function as a superposition of two Gaussians centered around the densities $\rho_{\rm gas}$ and $\rho_{\rm liq}$ of the coexisting gas and liquid phases. The relative weights of the two phases are fixed according to the lever rule of statistical mechanics. The relation (7) is *not exact* even within the limit $L \gg \xi$, since interfacial free energy contributions are neglected. However, this relation is a *reasonable approximation* not too close to the critical point, and especially at the outer wings of the P_L peaks. Using the coexistence densities of the high- and low-density phases, we define the order parameter as

$$\Phi(T) = \rho(T)_{\rm liq} - \rho(T)_{\rm gas}, \tag{8}$$

where we include the temperature dependence explicitly in the notation.

The quantity helping to locate the critical point in the phase diagram is the reduced fourth-order density cumulant,[39,40,36] which we denote as U_L,

$$U_L(T,\rho) = 1 - \frac{\langle(\Delta\rho)^4\rangle_L}{3\langle(\Delta\rho)^2\rangle^2_L}, \tag{9}$$

and U_L is zero for the Gaussian distribution (5) as is well known. Of course, there are corrections to this result, since $\langle(\Delta\rho)^4\rangle_L$ differs from $3\langle(\Delta\rho)^2\rangle^2_L$ by a connected part of a four-particle correlation function. Thus we can write for this case

$$U_L = L^{-d}\frac{\chi^{(4)}_L}{3(K^{(L)})^2}, \tag{10}$$

where $\chi^{(4)}_L$ tends to a finite nonzero constant as $L \to \infty$ and obviously vanishes for infinite block size. Below the critical point, in the regime of the bimodal distribution, the cumulant no longer vanishes due to the distinctly non-Gaussian character of P_L.

In the vicinity of the critical point (T_c, ρ_c), i.e., for $L \leq \xi$, the above presented formulas based on the Gaussian approximation are no longer valid. There the distribution function is already distinctly non-Gaussian in the one-phase region and interfacial contributions near the critical point play a non-negligible role. The analogy between off-lattice fluids and lattice gas models suggests one postulates a scaling form for the density distribution P_L. We will not discuss this aspect in detail, but rather refer the reader to Refs. 36 and 39, and concerning the special features of the cumulant method for off-lattice fluids to Ref. 37. However, it should be noted here that interfacial contributions *inside* the blocks on any length scale are completely neglected in deriving the corresponding formulas. With the above assumptions, a scaling form for the cumulant

$$U_L = f_u\{(\bar{\rho}-\rho_c)|\epsilon|^{-\beta}, L|\epsilon|^{\nu}\} \tag{11}$$

can be written down; f_u is a scaling function, $\epsilon = 1 - T/T_c$, $\xi \sim |\epsilon|^{-\nu}$, and β and ν are the critical exponents of the order parameter and correlation length, respectively. Similar relations can be derived for the moments of the density distribution and the compressibility.[36]

Of particular interest for us is the case $\bar{\rho} = \rho_c$, where the scaling function f_u has only the single argument $L|\epsilon|^{\nu}$. In the well-known case of lattice systems[39,40] at the critical point, the cumulants U_L must intersect in a common intersection point $U^*(T_c,\rho_c) = f_u(0,0)$ independent of the block length L. Locating such an intersection point can be used as a criterion to find T_c. In case of the fluid models, a similar procedure also seems to work: as shown in some cases,[36,37,27] the cumulants merge together near the (tri)critical point. In the present model, the situation of having to locate the critical point of the gas-liquid coexistence line is facilitated by the fact that this point is a common *tricritical* point of a second- and first-order transition. This second-order transition, which ends at the tricritical point, is the magnetic transition from the paramagnetic to the ferromagnetic fluid phases at a density $\rho_c(T > T_c)$. In case of a usual critical point for off-lattice fluids, more elaborate methods[37] have to be devised to locate *simultaneously* critical density and temperature.

In principle, the density cumulants can also be used to locate the triple point, as will be introduced in this paragraph. Note that in the limit $N \to \infty$, $L \to \infty$ such that $N/L^d \to \infty$, where interfacial contributions to the cumulants in two-phase regions are negligible,[37] the cumulant U_∞ is simply expressed in terms of the volume fraction x (or x') of the gas phase[36]

$$U_\infty(x^{(\prime)}) = \frac{6\,x^{(\prime)} - 1 - 6\,x^{(\prime)\,2}}{3\,x^{(\prime)}(1-x^{(\prime)})} \tag{12}$$

in the gas-liquid (gas-solid) coexistence region. We define the volume fraction of the gas phase above the triple temperature as

$$\bar{\rho} = \rho_{\mathrm{liq}} + (\rho_{\mathrm{gas}} - \rho_{\mathrm{liq}})\, x \tag{13}$$

and below the triple temperature as

$$\bar{\rho} = \rho_{\mathrm{sol}} + (\rho_{\mathrm{gas}} - \rho_{\mathrm{sol}})\, x' , \tag{14}$$

see Fig. 2 for a geometrical definition of these quantities. Formula (12) is obtained by replacing the two normalized Gaussians in (7) by two δ functions centered around the coexisting densities and using the definition (9) of the cumulant. The rectilinear diameter is obtained for $x = 1/2$. The same argument leading to the Gaussian approximation (7) to describe the gas-liquid coexistence above a triple temperature goes through for the coexistence of a gas with a solid below this triple temperature, and the same ideas apply for considering its cumulant. The only difference is that the solid has in general a different density than the liquid does, i.e., ρ_{liq} has to be replaced by $\rho_{\mathrm{sol}} = \rho_{\mathrm{liq}} + \Delta\rho$ in (7), with the density jump $\Delta\rho$, see Fig. 2. As a consequence, a discontinuity due to the different liquid and solid coexistence densities (the gas density practically does not change in the tiny temperature interval considered around the triple temperature) occurs at the triple temperature T_t. Since we can, in the above-defined limits, give a closed expression (12) for the cumulants $U_\infty(x^{(l)})$ as a function of the rectilinear diameter in the gas-liquid and gas-solid coexistence regions, and since just this quantity changes discontinuously at T_t, the cumulants themselves have to possess a kind of discontinuity at T_t. Exactly at the triple point, three Gaussians have to be combined according to the lever rule. In the case of finite systems, the sharp behavior of U will be smeared out. We expect a sign change of the cumulants' curvatures occurring at a common point for all L, and that this circumstance can be exploited to obtain an estimate for the triple temperature. Thus by extension of the known gas-liquid density block analysis technique to the gas-solid transition, one can in principle extract the triple point temperature and the solid phase coexistence densities in a canonical simulation without possibly imposing boundary constraints on the system.

Having devised techniques to locate the (tri)critical and triple points in a phase diagram using the density distribution in subblocks, we now outline the extraction of

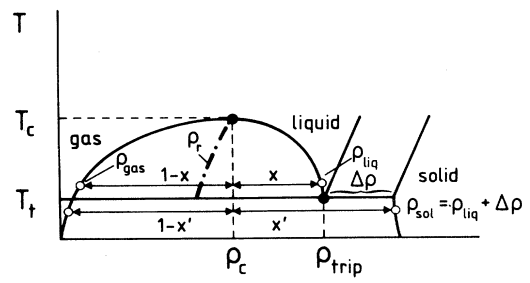

FIG. 2. Schematic phase diagram of the fluid system. For symbols and explanations see text.

the isothermal compressibility K in the thermodynamic limit. Sufficiently far away from the critical point, i.e., $L \gg \xi$, where (5) and (7) are supposed to hold, the *effective* compressibility $K^{(L)}$ defined from either the second moment of the density fluctuations in the subblocks (6), or from the half width of the distribution (5), will differ from the physical compressibility K, resulting in the thermodynamic limit. In leading order, we expect[36] that K and $K^{(L)}$ differ by a *boundary correction*

$$K^{(L)} = K\left[1 - K^{\mathrm{bc}}\left(\frac{\xi}{L}\right)\right], \quad L \gg \xi. \tag{15}$$

Thus a quantity closely related to particle fluctuations can be estimated reliably also in the usual *canonical ensemble* where the total number of particles is fixed, if only the fluctuations are studied in subsystems. The justification of (15) is presented in Ref. 36 and will not be given here.

There are, as usual, several limitations and drawbacks of the proposed method which we do want to discuss. In practice, the simulations consider rather small block sizes L, where many of the relations written down here are not yet strictly valid. The relation (11) is valid only in the limit $L \to \infty$, $\xi \to \infty$, L/ξ finite, and disregards corrections to finite-size scaling, see Ref. 39. And even far from the critical regime, the Gaussian approximation suffers from boundary effects,[36] i.e., contributions depending on a surface to volume ratio $\propto \xi/L$ as in (15). In addition, there are interfaces *inside* the subsystems, which are neglected in our approach. These limitations are investigated and discussed in Ref. 37, where an extensive study of the 2D Lennard-Jones fluid with 4096 particles is provided.

Finally, we want to draw attention to some technical aspects, i.e., how to implement the presented method if only very small systems (as in the present study) can be simulated. First of all, the "useful" size L of the blocks is limited from below and above: the usual requirement $\xi \ll L$ has to be met and in addition the blocks have to represent *quasi-grand-canonical ensembles* to allow for independent density fluctuations, i.e., $L \ll S$ also has to be satisfied. It does not make any sense to use very small blocks having the size of the hard disk diameter or large blocks with $M_b = 2$, since in this case the periodic boundary conditions couple the four blocks and the resulting density fluctuations are by no means uncorrelated. Thus the window of useful block sizes has to be determined beforehand, making *compromises between pragmatism and purism.*

Another aspect concerns the accurate extraction of the positions and widths of the peaks of P_L yielding the coexistence densities and compressibilities. The most reliable procedure consisted of fitting the simulation-P_L data points by Gaussians with variable mean, width, and area. In the bimodal regime, only the outer wings of the gas and liquid P_L peak are fitted *independently*, thus minimizing the effect of interfacial contributions. It is not advisable to do a simultaneous fit of the bimodal P_L over the total density range, using two (even independently) weighted Gaussians as suggested by (7), whereas fitting all simulation points with (5) works well above

the (tri)critical point. Only the cumulants are calculated from P_L using definition (9) directly. But despite the mentioned delicacies, the results presented in Sec. IV are encouraging and illustrate that 200 particles are already enough to extract quite a lot of rather accurate thermodynamic information, if conventionally generated simulation data are evaluated by sophisticated methods. Especially in case of quantum simulations, where the system sizes are necessarily restricted to rather small particle numbers compared to state of the art classical simulations, such a finite-size-scaling approach is quite useful.

To close this section, the second type of ordering in our system, the transition from a paramagnetic fluid to a ferromagnetic fluid, is discussed in the light of the block analysis. The distribution functions of the magnetization in subsystems can be analyzed in analogy to corresponding work[39] on lattice models. Again, we divide the system into blocks as for the density, but now we measure the z magnetization m_i (see Sec. III B) in the ith subsystem to obtain the magnetization distribution function $\tilde{P}_L(m)$ for a given length L of the blocks

$$\langle m^k \rangle_L = \int m^k \tilde{P}_L(m) dm, \tag{16}$$

where $\tilde{P}_L(m)$ is the average of the magnetization distributions $\tilde{P}_L(m_i)$ for all blocks $i = 1, \ldots, M_b^d$. This procedure is visualized in Fig. 1 where a few "ferromagnetic boxes" with mostly "spin-up" clusters and others with "spin-down" regions can be identified in addition to "paramagnetic subsystems" where the particles' magnetic moments annihilate. The analysis of the cumulants on different length scales leads to a better estimate of the magnetic transition than just taking the maximum of the susceptibility peak as done in the present study. But note that, contrary to ρ_i, now the basic variable m_i is the sum of all average magnetic moments of the particles in the ith block which can be positive or negative. Thus near the magnetic transition, substantial cancellations will lead to large statistical errors in the measured quantity $\tilde{P}_L(m_i)$. From the experience with lattice systems,[39,40] we feel that a 14×14 particle system like ours with additional underlying density fluctuations (i.e., the magnetization in a block can change due to spin flips and due to diffusive motion of the particles) is not large enough to allow for an honest finite-size study. Now we shall proceed to describe how the PIMC simulations were done.

B. Path-integral Monte Carlo simulation

Due to the adiabatic approximation, our classical-quantum canonical distribution function is the product of a trivial classical momentum part, which is integrated out to yield the thermal de Broglie wavelength λ, and N-particle density matrix.[19] This density matrix is most easily handled by considering the partition function in the PIMC formalism

$$\begin{aligned} Z(\beta, N, V) &= \lambda^{-2N} \frac{1}{N!} \int d\mathbf{r}_1 \cdots \int d\mathbf{r}_N \mathrm{tr}_\sigma \exp(-\beta \hat{V}) \\ &= \lim_{P \to \infty} Z_P(\beta, N, V) \end{aligned} \tag{17}$$

and for an introduction to PIMC methods we refer the reader to Refs. 29–35. Following Suzuki,[44] we use the Trotter formula to discretize the partition function in the Trotter dimension P as[19]

$$Z_P(\beta, N, V) = \frac{A_P^{NP}}{\lambda^{2N} N!} \int d\mathbf{r}_1 \cdots \int d\mathbf{r}_N e^{-\beta \sum_{i<j} U(r_{ij})} \sum_{\{S\}} e^{-\beta \mathcal{V}_P(\{S\})}. \tag{18}$$

The temperature dependent effective potential is defined as

$$-\mathcal{V}_P(\{S\}) = \sum_{i=1}^{N} \sum_{p=1}^{P} \left(K_P S_{i,p} S_{i,p+1} + \frac{1}{P} \sum_{j=i+1}^{N} J(r_{ij}) S_{i,p} S_{j,p} \right), \quad S_{i,p} = \pm 1, \tag{19}$$

where

$$\begin{aligned} A_P &= [\tfrac{1}{2} \sinh(\beta\omega_0/P)]^{1/2}, \\ K_P &= \frac{1}{2\beta} \ln[\coth(\beta\omega_0/2P)]. \end{aligned} \tag{20}$$

Cyclic boundary conditions due to the trace operation $S_{i,P+1} = S_{i,1}$ close the paths. The P-dependent properties of the system can now be obtained as thermal averages $\langle \ \rangle_P$ with the effective classical canonical distribution of the $N \times P$ particles

$$\propto \exp[-\beta \mathcal{H}_P(\beta)] = \exp\left(-\beta \sum_{i<j} U(r_{ij}) - \beta \mathcal{V}_P(\{S\}) \right) \tag{21}$$

using the standard Metropolis Monte Carlo method[42,43] in the NVT ensemble; $S_{i,p}$ are classical Ising spin variables of particle number i at imaginary time slice p. In analogy to the path integral in continuous Cartesian space, the "kinetic part" of the Hamiltonian is identified by the coupling $\sim S_{i,p} S_{i,p+1}$ of the classical spins of a given particle i between two neighboring time slices p and $p+1$ suggesting the ring-polymer language,[29,31,34] whereas the potential contribution of two particles i and j has to be evaluated at the same time slice $\sim S_{i,p} S_{j,p}$. Again, the coupling constant K_P occuring in the "kinetic part" is temperature dependent.

The next step consists of defining the estimators[32] for thermodynamical observables as energy, magnetization, etc., which can be obtained by the usual derivatives of the partition function Z_P for a given Trotter discretization. The total energy estimator is defined as

$$\langle E \rangle_P = \langle E^{\mathcal{T}} \rangle_P + \langle E^{\mathcal{V}} \rangle_P, \tag{22}$$

where

$$\langle E^{\mathcal{T}}\rangle_P = -\frac{\omega_0}{2}\left\{N\tanh^{-1}\left(\frac{\beta\omega_0}{P}\right) - \sinh^{-1}\left(\frac{\beta\omega_0}{P}\right)\left\langle \sum_{i=1}^{N}\frac{1}{P}\sum_{p=1}^{P} S_{i,p}S_{i,p+1}\right\rangle_P\right\} \tag{23}$$

and

$$\langle E^{\mathcal{V}}\rangle_P = -\left\langle \sum_{i<j}^{N} J(r_{ij})\frac{1}{P}\sum_{p=1}^{P} S_{i,p}S_{j,p}\right\rangle_P, \tag{24}$$

a possible alternative energy estimator is the one based on the virial.[45] We did not include the trivial classical translations of the particles which only result in the thermal de Broglie wavelength in the above-defined total energy and related quantities. Similarly, the corresponding heat capacity estimator

$$\langle C_v\rangle_P = \langle C_v^{\text{fluct}}\rangle_P + \langle C_v^{\text{ex}}\rangle_P, \tag{25}$$

where

$$\langle C_v^{\text{fluct}}\rangle_P = \beta^2\{\langle E^2\rangle_P - \langle E\rangle_P^2\} \tag{26}$$

and

$$\langle C_v^{\text{ex}}\rangle_P = \beta\left\{\langle E^{\mathcal{T}}\rangle_P\left(\frac{\beta\omega_0}{P}\right)\coth\left(\frac{\beta\omega_0}{P}\right) + N\frac{\omega_0}{2}\left(\frac{\beta\omega_0}{P}\right)\right\} \tag{27}$$

can be written down[46] for an effective Hamiltonian $\mathcal{H}_P$ being temperature dependent. The total magnetization measured in the z direction is

$$\langle M\rangle_P = \left\langle \sum_{i=1}^{N}\frac{1}{P}\sum_{p=1}^{P} S_{i,p}\right\rangle_P \tag{28}$$

and

$$\langle \chi\rangle_P = \beta\left\{\left\langle\left[\sum_{i=1}^{N}\frac{1}{P}\sum_{p=1}^{P} S_{i,p}\right]^2\right\rangle_P - \left\langle \sum_{i=1}^{N}\frac{1}{P}\sum_{p=1}^{P} S_{i,p}\right\rangle_P^2\right\} \tag{29}$$

is the isothermal magnetic susceptibility. The total imaginary time correlation functions are defined as

$$\langle C_z(\tau)\rangle_P = \left\langle \sum_{i=1}^{N}\frac{1}{P}\sum_{p=1}^{P} S_{i,p}S_{i,p+l}\right\rangle_P \tag{30}$$

and

$$\langle C_x(\tau)\rangle_P = \left\langle \sum_{i=1}^{N}\frac{1}{P}\sum_{p=1}^{P}\exp[-2\beta K_P(S_{i,p}S_{i,p+1} + S_{i,p+l}S_{i,p+l+1})]\right\rangle_P, \tag{31}$$

where $\tau = \beta l/P$ is the imaginary time. These correlation functions give information[19] about the degree to which the system is in "eigenstates" of $\hat{\sigma}^z$ or $\hat{\sigma}^x$. In the following parts, we study the properties $\langle\mathcal{O}\rangle^\star = \langle\mathcal{O}\rangle/N$ normalized per particle.

As obtained by a quite general analysis,[47] the errors of these first-order approximant[32] estimators for a Hermitian breakup of the Hamiltonian behave in leading order as

$$\langle\mathcal{O}\rangle_P = \langle\mathcal{O}\rangle_\infty + \frac{\mathcal{O}^{\text{corr}}(\beta)}{P^2} \tag{32}$$

for fixed temperature and system size. This Trotter scaling relation was used to check the dependence of the calculated observables on the special choice of P.

In order to study the features of the model described by (18) quantitatively, we performed for different densities (coverages) and temperatures PIMC simulations for a parameter set ($J = 1$, $R = 1$, $\omega_0/J = 4$) fixed to settle the system in the quantum regime; from now on we shall use the dimensionless temperature $T^\star = (\beta J)^{-1}$ and density $\rho^\star = \rho R^2$ and the overbar on $\rho^\star$ defines as before the density of the overall system. The number of classical particles N was 200 and the Trotter dimension P was chosen such that $T^\star P \approx 40$ for each temperature; the maximum P necessary was as large as 800. This choice of P appeared to be sufficient as tested by Trotter scaling various observables: doubling of P changed these observables only in the limits of the statistical error bars. We have chosen representative state points out of the two fluid phases, the coexistence region, and from near the critical line to make sure that no P influence of the phase behavior is present. As an additional independent crosscheck, we compared the PIMC imaginary time $\hat{\sigma}^z$ correlation functions with these functions from a virial expansion for low densities where this expansion is exact, see Sec. III C. In Fig. 3 the $C_z(\tau)$ PIMC data points for $\bar{\rho}^\star = 0.1$ fall nicely on the analytical curve demonstrating that the asymptotic Trotter limit is reached with $T^\star P \approx 40$; please note that the statistical effort is not high enough to extract smooth $C_x(\tau)$ curves from the simulation since these functions are related to the number of kinks along the imaginary time axis. In the following we will no longer distinguish between the averages of the estimators and the observables, assuming that P is large enough to assure the proper convergence of the Trotter decompositions.

Since the spin-spin coupling constant K_P stiffens with increasing P for fixed β, care has to be taken in the algorithm to allow for efficient MC dynamics[48] in the spin space even at low temperatures. We solved this problem by performing a whole cascade of local and global spin moves after the usual displacement of a randomly chosen particle in 2D Cartesian space. Each cascade con-

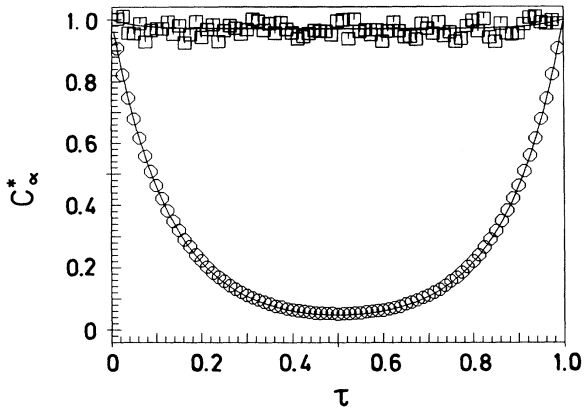

FIG. 3. Imaginary time correlation functions $C^*_\alpha = C_\alpha/N$ as a function of τ. Full lines, low-density expansions. Circles, PIMC results for C^*_z; squares, PIMC results for C^*_x. ($N = 200$, $\omega_0/J = 4$, $J = 1$, $T^*P \approx 40$, $T^* = 0.5$, $\bar{\rho}^* = 0.1$.) No error bars are shown.

sisted of the following sequence of four steps for all state points, flipping: (i) one single spin $S_{i,p}$, (ii) a whole chain, (iii) half of a chain, and (iv) a chain-segment where spin, particle, starting time slice, and length of the segment were chosen randomly. We call these four steps (together with the particle move in 2D) one MC step (MCS) per particle. With this setup we observed unexpectedly fast relaxation times at all the state points in the phase diagram presented in this paper. No more than 150 000 MCS were necessary at any state point, whereas in similar MC simulations[36] of a classical Lennard-Jones fluid in 2D with 256 or 576 particles, more than 500 000 MCS were needed in the coexistence region to build up the equilibrium two-peak structure of the density distribution, and 1 000 000 MCS had been used for thermalization starting from a square lattice. The very thorough study of the same fluid by Bruce and Wilding[26] calls for even longer equilibrations and simulations very near the critical point, with on the average 400 particles. Our equilibration time of $\approx 25\,000$ MCS was estimated to be sufficient by monitoring the temporal behavior of the total energy and density cumulants.

Using standard Monte Carlo techniques,[42,43] we computed expectation values of internal and interaction energies, magnetization, and susceptibility. The heat capacity is calculated directly from the energy estimator fluctuations supplemented with the correct excess term [due to the temperature dependence of the effective Hamiltonian in (19)] using the formulas presented, as discussed in Ref. 46. The main point is the detailed study of the density distribution functions $P_L(\rho)$ with which to determine the coexistence boundaries, as well as the compressibilities $K^{(L)}$ via scaling. The second-order magnetic transition is determined only roughly by considering the cusp in the susceptibility for the given system size. Even with this simplification, more than 400 CPU hours on a CRAY-YMP were necessary to obtain the results presented in this communication; a typical run with 100 000 MCS took about 4 h CPU time.

C. Analytical methods

Mainly to check the PIMC results, we also performed MF calculations of the model, which are shown as dotted lines in some of the presented graphs as a function of density. The Hamiltonian of the MF version of our model is defined as in 3D (Ref. 19) and reads for 2D coordinates

$$\hat{H}^N_{\mathrm{MF}} = \sum_{i=1}^{N} \frac{\mathbf{p}_i^2}{2\mu} - \frac{\omega_0}{2} \sum_{i=1}^{N} \hat{\sigma}_i^x, + \sum_{i<j} U(r_{ij}) - \frac{J_0}{N} \sum_{i<j} \hat{\sigma}_i^z \hat{\sigma}_j^z, \tag{33}$$

where the interaction between the internal degrees of freedom of two particles $(J_0/N)\hat{\sigma}_i^z\hat{\sigma}_j^z$ is now distance independent. Following Stratt,[18] the value of the averaged coupling constant J_0 is chosen to be

$$J_0 = \rho \int d\mathbf{r}\, J(r) g(r) \tag{34}$$

with the two-point correlation function $g(r)$. In the 2D case under consideration here, we have to approximate the true $g(r)$ and thus take for the homogeneous fluid system the Percus-Yevick (PY) approximation for hard disks.[49] We do not present further details of the MF theory such as, e.g., the corresponding free energy, but refer the reader to Ref. 19.

Paramagnetic behavior is obtained only as long as $\beta \leq \beta_c$, where β_c is given by the solution of

$$\frac{2J_0}{\omega_0} \tanh\left(\frac{\beta_c \omega_0}{2}\right) = 1, \tag{35}$$

which results from the self-consistency equation for the magnetization. No transition to a ferromagnetic phase takes place if $J_0 \leq \omega_0/2$, whereas for $J_0 > \omega_0/2$ and $\beta > \beta_c$ a ferromagnetic phase exists. Contrary to classical PY hard disks,[49] the free energy in our MF model is not a convex function of the density for all β. By taking the convex envelope of the free energy, this implies an additional first-order transition at low temperatures, i.e., liquid-gas coexistence in 2D.

The MF calculations were very useful in determining the choice of the quantum parameter ω_0/J in order to settle the expensive PIMC simulations in the genuine quantum region. In Fig. 4 we show the MF phase diagram for three choices of ω_0/J. This comparison prompted us to fix $\omega_0/J = 4$ for the extensive numerical study. As is well known, strong statistical fluctuations in 2D lead to considerable deviations from MF theory in all systems with short range forces, and thus Fig. 4 can only provide a qualitative picture.

As already mentioned, a virial expansion served us as a check of the simulation for very low densities. The analogy between the 3D and 2D cases is even closer than for the MF theory, so that we do not present any details but refer to Ref. 19. We used the imaginary time correlation functions obtained from a second-order low-density expansion and compared for very low densities (where the expansion is asymptotically exact) to these correlation functions obtained from PIMC, see Fig. 3 and Sec. III B. Concerning the quantum nature of the fluid at low den-

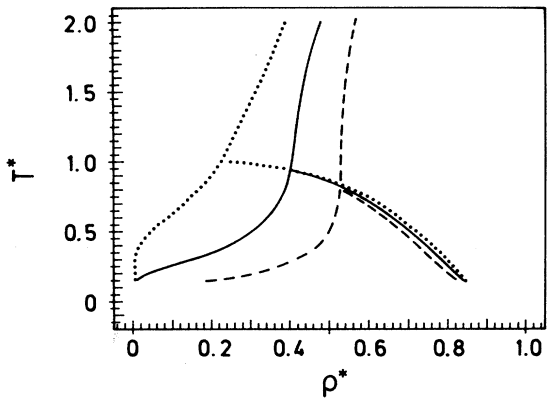

FIG. 4. Mean-field phase diagram ($J = 1$). Dotted line, $\omega_0/J = 0$; full line, $\omega_0/J = 4$; dashed line, $\omega_0/J = 6$.

sities, the advantage of the virial expansion is that it is exact to all orders, which means that we can check low-density PIMC data for their Trotter convergence.

IV. RESULTS AND DISCUSSION

A. Density distributions and compressibilities

The very essential data of the present investigation are the density distribution functions P_L for different length scales. In Fig. 5 we present such raw data for two temperatures and the five different length scales we used; the lines are linear connections of the simulation data. One can clearly distinguish the *supertricritical region* in (a) where the density distribution shows the expected unimodal behavior and the *coexistence region* in (b) with the bimodal P_L. At lowest (highest) temperatures, the shape of the distribution can be well approximated with two (one) Gaussians centered at the liquid and gas (overall) densities, as suggested by relation (7) [(5)]. As expected, the regime around the tricritical point is distinctly *non-Gaussian* due to large interfacial contributions. These effects are size dependent as clearly seen in Fig. 5(b): the peaks become better separated on large subsystem sizes (M_b small), and the features of the distribution vanish with decreasing block length. This behavior of the order parameter distribution function is characateristic[43] for *first-order transitions*, whereas for second-order transitions, one peak is built up at the expense of the other for increasing system size. Note that the positions of the peak maxima, corresponding to the gas and liquid coexistence densities, are nearly size independent not too close to the tricritical point; the widths of the peaks however are strongly dependent on M_b.

In order to extract the gas (liquid) coexistence density in the case of bimodal distribution, we fitted only the low- (high-) density wing of P_L up to the maximum by a single Gaussian on the five length scales shown in Fig. 5. In view of the irregular dependence of the extrema on L, we simply took the mean value to estimate the coexistence densities. Despite the fact that in principle one simulation run is sufficient to extract data on both coexisting phases, it turned out to be indispensable to perform two simulations, one close to the gas and the other close to the liquid side, to obtain reliable results for the coexistence densities near the tricritical point. Naturally there crops up the *problem of metastability*[50] if the quench density is located in between the spinodal and binodal lines. Out of this region, the system evolves via *heterophase fluctuations*, i.e., droplet formation is necessary. In case that no critical droplet is built up (which is a slow process in simulation) one can be misled to believe that the parameters have settled the system in a stable one-phase region. If the system is quenched out of a state in the instability region in the phase diagram, the relaxation to the equilibrium distribution occurs with *homophase fluctuations*, i.e., small amplitude and long wavelength instabilites, via "uphill diffusion," to the equilibrium composition. The consequence for the simulation is to check configurations and the temporal behavior of the P_L peak maxima, to make sure that the system is really phase separated if the quench density is situated near a coexistence density.

In the fluid phase, see Fig. 5(a), the major influence of the system size is to alter the width of the Gaussian and thus the *effective compressibility* $K^{(L)}$. To demonstrate

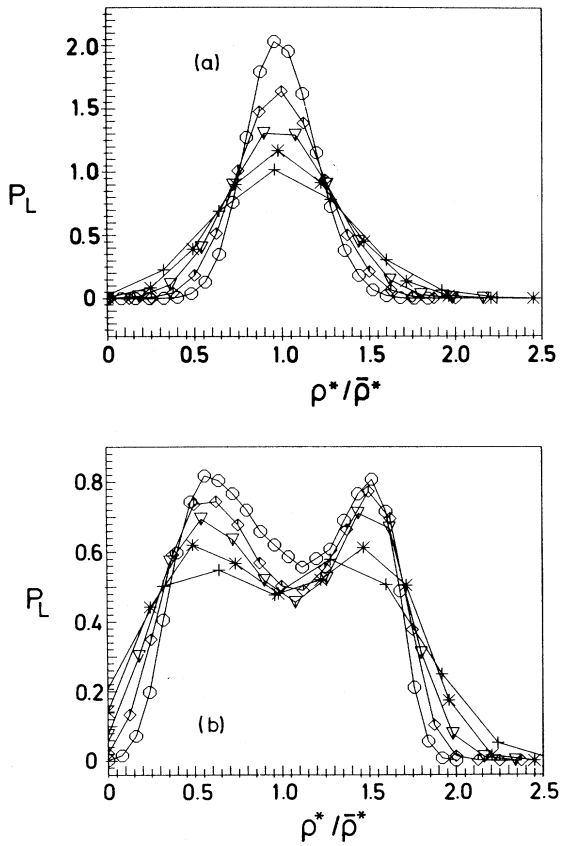

FIG. 5. Normalized block density distributions P_L as a function of $\rho^*/\bar{\rho}^*$ for different subsystem sizes $M_b = \{4$, circles; 5, diamonds; 6, triangles; 7, stars; 8, crosses$\}$. ($\omega_0/J = 4$, $J = 1$, $N = 200$, $T^*P \approx 40$.) (a) Supertricritical region at $T^* = 0.7$ and $\bar{\rho}^* = 0.45$. (b) Subtricritical region at $T^* = 0.4$ and $\bar{\rho}^* = 0.45$. Connecting lines are for visual help only.

this behavior, we present in Fig. 6 the raw simulation data with fitted Gaussians for three blockings. Thus the assumption of Gaussian behavior, on which major parts of the analysis are built, is fulfilled in the investigated regions of our 200 particle system for the used subsystem sizes. The effective compressibilities $K^{(L)}$, as shown in Fig. 7 for one temperature, are obtained from the fitted width parameters, see Fig. 6, as defined in (5). On the basis of the effective compressibilities for a set of blockings, we extrapolate the *physical compressibility* K in the thermodynamic limit, using (15) as shown in Fig. 7 for a couple of densities at $T^\star = 1.0$. Note that for the given overall system size only the subsystems corresponding to $M_b = 4$, 5, 6, 7, and 8 could be used to produce meaningful results; if much larger sytems are used, this window of useful blocks can be extended as done in Ref. 37 for 4096 (purely classical) particles. In the chosen window the effective compressibilities scale, as expected, with the surface-to-volume ratio $\propto 1/L \propto M_b$, see Fig. 7. The resulting *extrapolated* physical compressibilities for a whole density scan at $T^\star = 1.0$ are shown in Fig. 8(a); we also present the subsystem size dependent $K^{(4)}$ for the largest blocks with $M_b = 4$ in the same frames for comparison. The extrapolated PIMC data agree well with the MF prediction at low and high densities. If $K^{(L)}$'s are used as an estimate for K, the deviations from MF are systematically larger and thus the extrapolation of $K^{(L)}$ to the infinite system is crucial to eliminate the boundary effects. The compressibilities as a function of $\bar{\rho}^\star$ indicate a kink singularity (or possibly a small cusp) at $\bar{\rho}^\star \approx 0.54$, which is not predicted by MF: this anomaly is already an indication of a phase transition in the fluid phase. As will be discussed in more detail in Sec. IV B, a low-density paramagnetic fluid changes with increasing density *continuously* in a ferromagnetic fluid at $\bar{\rho}^\star \approx 0.54$ for $T^\star = 1.0$, exactly where the kink in $K(\bar{\rho}^\star)$ is located. The compressibility in the paramagnetic phase seems to saturate before reaching the phase transition, and then it falls upon switching on the spin-spin coupling to nearly

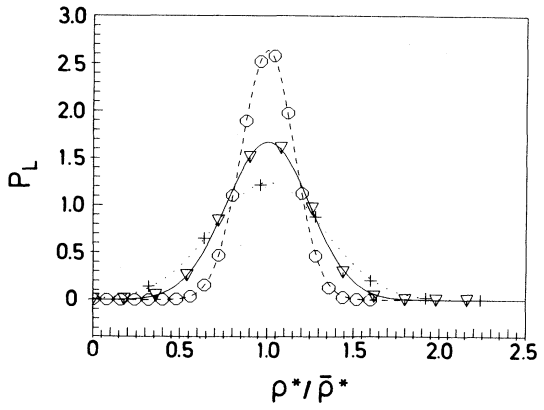

FIG. 6. Normalized block density distributions P_L as a function of $\rho^\star/\bar{\rho}^\star$ at $T^\star = 1.0$ for different subsystem sizes M_b = {4, circles; 6, triangles; 8, crosses}. ($\bar{\rho}^\star = 0.55$, $\omega_0/J = 4$, $J = 1$, $N = 200$, $T^\star P \approx 40$.) The lines are fitted Gaussians as indicated in the text.

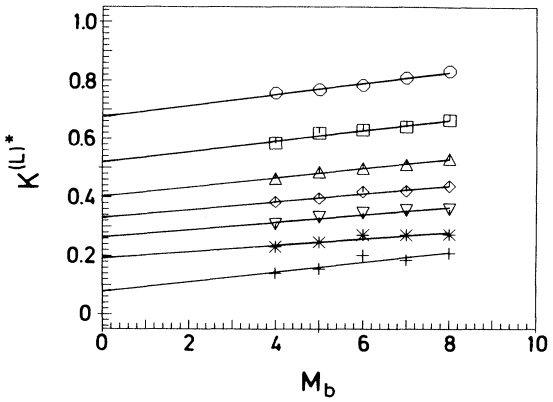

FIG. 7. Isothermal compressibility $K^{(L)\star} = \bar{\rho}K^{(L)}/\beta$ in the fluid phase as a function of the subsystem size M_b for different densities $\bar{\rho}^\star$ = {0.1, circles; 0.2, squares; 0.3, up-triangles; 0.4, diamonds; 0.5, down-triangles; 0.6, stars; 0.7, crosses}. ($T^\star = 1.0$, $\omega_0/J = 4$, $J = 1$, $N = 200$, $T^\star P \approx 40$.) The full lines are linear fits. Error bars are smaller than the size of the symbols.

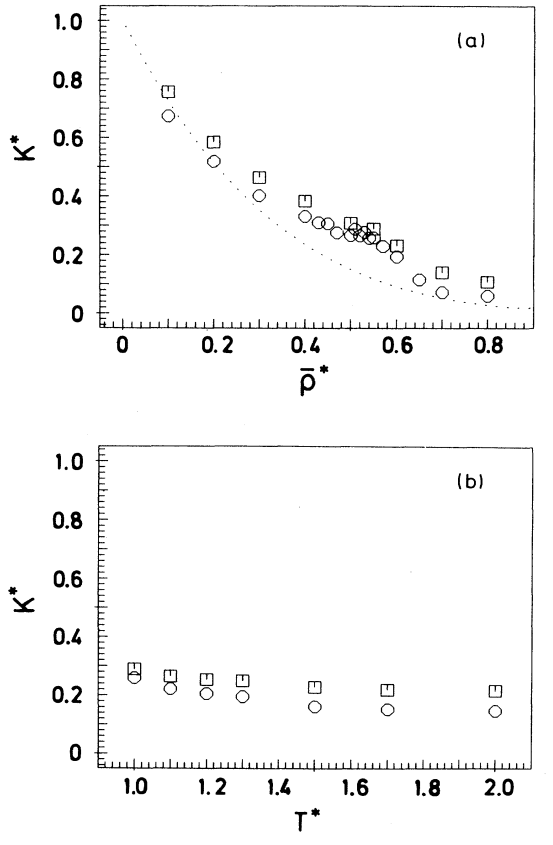

FIG. 8. Isothermal compressibility $K^\star = \bar{\rho}K/\beta$ in the fluid phase ($\omega_0/J = 4$, $J = 1$). Dotted line, MF prediction; circles, PIMC results for $K^{\infty\star}$; squares, PIMC results for $K^{(4)\star}$. ($N = 200$, $T^\star P \approx 40$.) (a) As a function of $\bar{\rho}^\star$ for $T^\star = 1.0$. (b) As a function of $T^\star$ for $\bar{\rho}^\star = 0.55$. Error bars are smaller than the size of the symbols.

zero in the magnetically ordered phase. This coupling between density correlations and spin correlations is not predicted by MF theory. In Fig. 8(b) we show the slowly decreasing compressibility with increasing temperature at the fixed density $\bar{\rho}^* = 0.55$. Of course, with a total number of 200 particles and much smaller particle numbers in our subsystems, we cannot make a real attempt to see the critical divergence of the compressibility as T approaches the tricritical point.

B. Phase transitions and phase diagram

In Fig. 9(a) we present the magnetization as a function of the density at the fixed temperature $T^* = 1.0$; we measure the magnetization in the z direction, see (28). This behavior is typical[42,43] for a *second-order magnetic transition* from a paramagnetic to a ferromagnetic phase (which is in our case a fluid phase) at higher densities. By increasing the density, the particles only start to effectively feel the distance dependent spin-spin coupling $\propto J(r_{ij})\hat{\sigma}_i^z\hat{\sigma}_j^z$ at densities exceeding a temperature dependent threshold. The decay of the magnetization with increasing thermal fluctuations can be seen in Fig. 9(b)

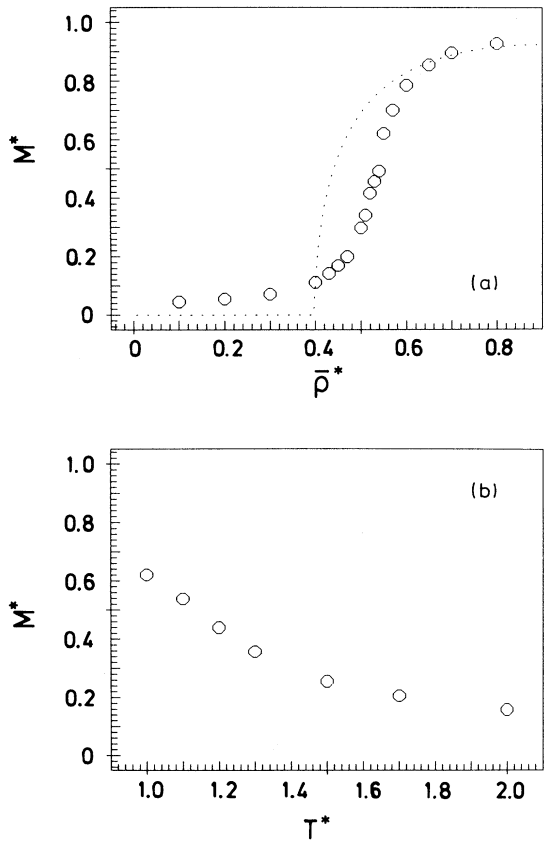

FIG. 9. Magnetization $M^* = M/N$ in the fluid phase ($\omega_0/J = 4$, $J = 1$). Dotted line, MF prediction; circles, PIMC results. ($N = 200$, $T^*P \approx 40$.) (a) As a function of $\bar{\rho}^*$ for $T^* = 1.0$. (b) As a function of T^* for $\bar{\rho}^* = 0.55$. Error bars are smaller than the size of the symbols.

for fixed $\bar{\rho}^* = 0.55$. The physical picture is that the *molecules acquire a dipole moment* due to the interactions with other molecules as a *cooperative effect*. A similar coupling of the density to an internal (magnetic) state is experimentally observed in O_2 layers on graphite.[12,13]

The trend seen in the magnetization is also manifest in the imaginary time correlation functions for low densities in Fig. 3. Along the z axis, the correlations decay rapidly for $T^* = 0.5$, indicating that the short range J coupling, aligning the spins in the z direction, is not efficient at that temperature; the correlations along the x axis are much stronger. With decreasing temperature, i.e., with increasing relative strength βJ of the spin-spin interaction, the correlation along the imaginary z direction increases. The buildup of z magnetization is a consequence of lifting the particles out of their internal $\hat{\sigma}^x$ ground state into a hybrid state by mixing with $\hat{\sigma}^z$ eigenstates. Thus the magnetic phase transition is the product of the *competition* of internal and collective properties in this many-body quantum system. Very roughly, the critical density $\bar{\rho}_c^*(T)$ where long range magnetic order appears can be estimated from the inflection point of the curve in Fig. 9(a) as $\bar{\rho}_c^*(T^* = 1.0) \approx 0.56 \pm 0.01$. Again, a small shift of this estimate due to finite-size effects is possible. One could try to refine such estimates by a subsystem analysis of the magnetization, as discussed at the end of Sec. III A, but with 200 particles only; we did not expect much more accuracy and thus did not undertake any attempts along these lines.

The heat capacity is also sensitive to the transition in the internal quantum states as illustrated in Fig. 10, in (a) as a function of the density for $T^* = 1.0$ and in (b) for fixed $\bar{\rho}^* = 0.55$; for experimental magnetocaloric effects of O_2 on graphite see Refs. 12 and 13. The scatter in the PIMC data is quite large, which has to do with the peculiar way this quantity has to be calculated using (25); further technical details are presented in Ref. 46. The peak in (a) separates the paramagnetic fluid with large energy fluctuations and correspondingly high heat capacity from the ferromagnetic fluid, where energy fluctuations are suppressed by the additional ordering effect in the internal degrees of freedom; a similar trend was already observed in the compressibility. From the universality principle, one might expect that this transition should fall in the same class as the 2D Ising model, and then the heat capacity should have a logarithmic divergence as $N \to \infty$. In this spirit, the peak in Fig. 10(a) could be interpreted as the finite-size rounding of this singularity. At $T^* = 1.0$, the heat capacity of the ferromagnetic fluid vanishes asymptotically for large $\bar{\rho}^*$, whereas the paramagnetic fluid has a nonzero, nearly constant heat capacity; please remember that we do not include the classical translational part of the heat capacity in our definition. Again the PIMC results in Fig.10(a) are in good agreement with MF predictions far away from phase transitions. In part (b) of this figure, the behavior of the heat capacity with increasing temperature can be followed. Again we see the signature of the second-order magnetic transition as a damped kink around $T^* \approx 1.2$.

The isothermal magnetic susceptibility is presented in Fig. 11 as a function of temperature for $\bar{\rho}^* = 0.55$. A

crude estimate for the critical line of the magnetic transition can be obtained by taking the maximum of the susceptibility in the finite system. By scanning the density at $T^* = 1.0$ we obtain $\bar{\rho}^* \approx 0.53 \pm 0.01$. The small difference with the above estimate from the inflection point of the magnetization reflects the finite-size effects: shifts of the critical point due to finite size are obviously rather small in our case. A more careful finite-size analysis of the magnetic transition, as discussed in Sec. III A, did not seem warranted in view of the required computer time. That is the way we determined the whole *critical line*, starting from the tricritical point and up to $T^* = 2.0$. As shown by very recent density functional calculations[51] on the same model, this critical line bends over at high temperatures to hit the fluid-solid coexistence region.

The liquid-gas coexistence boundaries were determined using the peak maxima of the density distributions as described in the previous section. The resulting phase diagram, the central highlight of this investigation, is presented in Fig. 12 together with the corresponding MF prediction. For temperatures above the tricritical point, there is only a fluid phase. However, the fluid may be paramagnetic or ferromagnetic, dependent on the density. Upon lowering the temperature, a gas phase can coexist with a liquid phase in a certain density window.

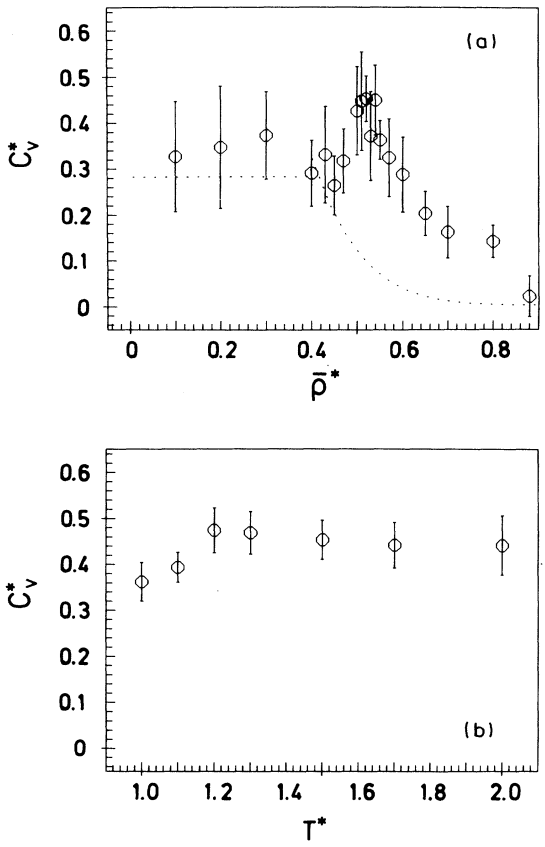

FIG. 10. Heat capacity $C_v^* = C_v/N$ in the fluid phase ($\omega_0/J = 4$, $J = 1$). Dotted line, MF prediction; circles, PIMC results. ($N = 200$, $T^*P \approx 40$.) (a) As a function of $\bar{\rho}^*$ for $T^* = 1.0$. (b) As a function of T^* for $\bar{\rho}^* = 0.55$.

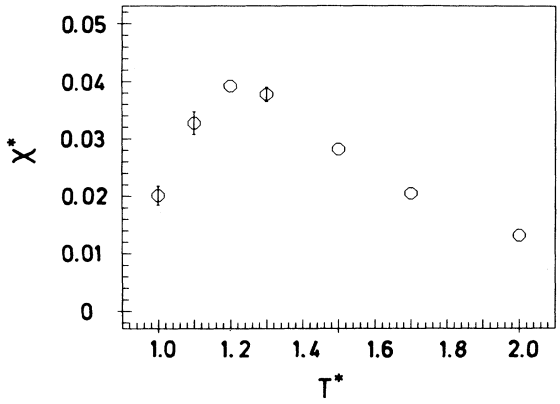

FIG. 11. Isothermal magnetic susceptibility $\chi^* = \chi/\beta N$ as a function of T^* for $\bar{\rho}^* = 0.55$ in the fluid phase ($\omega_0/J = 4$, $J = 1$). Circles, PIMC results. ($N = 200$, $T^*P \approx 40$.)

Since the preferred internal state at high (low) density is the (non-) magnetized fluid, these attributes are carried over to the coexisting phases: a paramagnetic gas coexists with a ferromagnetic liquid resulting in a *tricritical point.*

The qualitative dependence of the location of the tricritical point on the "quantum strength parameter" ω_0/J can be inferred from Fig. 4. One clearly sees that the phase diagram does not change qualitatively with increasing quantum character of the interactions. In general the only effect consists in a shift of transition temperatures and densities towards lower temperatures and higher densities; this is also true for the square lattice solid boundaries, see Ref. 51. Such a behavior is expected for a wide class of adsorbates, as, e.g., for orientational transitions of linear molecules on graphite.[11,58,59] In such a case of rotational motion, the moment of inertia (or the

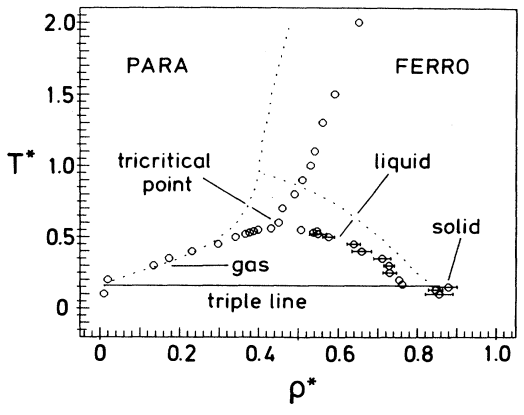

FIG. 12. Phase diagram ($\omega_0/J = 4$, $J = 1$). Dotted lines, MF prediction; circles, PIMC results ($N = 200$, $T^*P \approx 40$). Error bars are shown only when they exceed the size of the symbols. We believe that systematic errors do not exceed the size of statistical errors, except possibly in the close vicinity of the tricritical point. For further details see the text.

rotational constant) can serve as the quantum strength parameter of the problem. In the low-temperature limit, only the two lowest rotational states are occupied. This situation may be modeled using a kind of "few-level" approximation[11] similarly to the present study, which immediately leads to the identification of ω_0 with the level splitting (given by the rotational constant of the molecule) of the two lowest energy levels; the degeneracy of the excited levels has be considered. With increasing level splitting, quantum fluctuations become more important and drive the transitions (with other parameters kept fixed) to lower temperatures.[59] As qualitatively evident in Fig. 4, our simplified model Hamiltonian also shows these features. We determined the phase boundaries shifted due to quantum effects over a wide density range *quantitatively* for a given quantum strength, see Fig. 12.

Comparison of the phase diagram with the same Hamiltonian in three dimensions (3D), which is known mainly due to extensive analytical investigations,[19] is instructive. The Hamiltonian reveals the same topology of the phase diagram in 2D and 3D, i.e., a fluid phase, which can occur in a para- and a ferromagnetic internal structure, and paramagnetic gas and ferromagnetic liquid phases. The only effect of the decrease in the dimensionality is to shift the tricritical point towards lower temperatures and higher densities due to the larger fluctuations in 2D. Thus, all the phases "survive" upon lowering the dimensionality of the Hamiltonian, which is a nontrivial result. This means that the present model can be exploited, as shown in this investigation, to study general behavior of adsorbed layers[22] of molecules with internal quantum states. A wealth of experimental data[5] support the occurrence of similar phases in 2D physisorbed films as in the corresponding 3D bulk phases; however, solid phases in 3D are often replaced by registered phases in 2D. Thus incorporating an underlying corrugation potential acting on the classical coordinates $\{\mathbf{r}_i\}$ would be another interesting step towards the investigation of realistic systems based on the present Hamiltonian.

At this point, we want to stress that in the MF approximation, the spin correlations are factorized[19] by hand and their feedback effect on the fluid structure is neglected. This is the reason why no signature of the magnetic transition is seen in the MF result for the compressibility (Fig. 8). In 2D phase transitions there are always much stronger thermal fluctuations[1,2] than in 3D, and nontrivial correlations arise. Consequently, the MF approximation is accurate far from transitions only and the transition point cannot be estimated reliably by construction. In addition, it contains MF tricritical exponents which are correct in 3D (apart from logarithmic corrections to power laws), while rather different exponents[52] occur in 2D. As a result of these approximations, the MF tricritical temperature is off by a factor of 2 as compared to PIMC in 2D. In 3D, there are too few PIMC data[19] to judge how well the MF approximation does. But it is clear from the comparison of the performance of the MF approximation in 2D and 3D on quantities like magnetization or susceptibility, that the MF theory is much more accurate in 3D as expected. In the case of adsorbed layers of molecules, we do not think that MF calculations can serve as a *quantitative* comparison to experimental transition temperatures, even using realistic Hamiltonians.

But it should not be overseen that the MF predictions are a valuable tool with which to predict the general topology of phase diagrams even in 2D. Also in the present study, the MF calculation provides a *qualitatively* correct phase diagram; but this is not necessarily the case for repulsive forces of longer range, see Ref. 22. They serve in addition as an independent test of the PIMC results in certain limits. For quantities such as magnetization [Fig. 9(a)] and the response function susceptibility, heat capacity [Fig. 10(a)] and compressibility [Fig. 8(a)], we found close agreement between PIMC and MF in regions were the MF theory is supposed to work quantitatively, i.e., far away from any phase transitions.

C. Tricritical and triple point

An estimate of the tricritical temperature and density can be gained from the phase diagram, but we are also able to locate the tricritical point using properties of the density cumulants. In general, e.g., for a classical Lennard-Jones fluid, the critical density is unknown and has to be determined simultaneously[24–26,36,37] together with the temperature; in lattice gas models with pair interactions, the critical density is known by symmetry.[22] In our model, however, the tricritical density can be obtained by lowering the temperature and following the critical line until it merges into the gas-liquid coexistence curve. We estimated the tricritical point to be located at $\bar{\rho}^{\star}_{\mathrm{tri}} = 0.45 \pm 0.01$. Now we are in the position to perform a temperature scan at $\bar{\rho}^{\star}_{\mathrm{tri}}$ and to record $U_L(T^{\star}, \bar{\rho}^{\star}_{\mathrm{tri}})$ as done in Fig. 13(a). The block sizes corresponding to $M_b < 4$ and $M_b > 8$ do not satisfy the introduced consistency requirement $\xi \ll L \ll S$ on L and are not used for evaluation. At first sight, one can see in (a) the clustering of the cumulants on all length scales L at $T^{\star}_{\mathrm{tri}} \approx 0.6$. Above this temperature, the cumulants vanish asymptotically with increasing subsystem size, as expected from relation (10). In the blowup Fig. 13(b) it seems that we can locate the tricritical temperature by fitting the cumulants yielding a tricritical temperature of $T^{\star}_{\mathrm{tri}} = 0.57 \pm 0.02$; please note that the small system size does not allow a final conclusion concerning a universal fixed point of U. Upon lowering the temperature, the cumulants increase rapidly to reach a maximum value, and then fall off again.

It is instructive to follow the "flow of the cumulants"[39] along the $1/L$ axis depending on the temperature with fixed tricritical density in Fig. 14. As seen by following the (least-squares-) fitted linear curves in the graph, the cumulants are approximately independent of the length scale around a temperature $T^{\star}_{\mathrm{tri}}$, whereas they seem to have a block dependence above and below this temperature. This behavior is well known for Ising lattice models[39,40] and has been verified to a much higher accuracy. However, with only five different (and rather small) block sizes, a definite answer concerning the systematic L dependence of the cumulants in the vicinity of the tricritical point in this fluid system cannot be given. Of course, experience[39,40] supports that one should carefully

consider systematic errors due to the smallness of L. Because of prohibitively large computing time requirements for a large-L analysis, we were unable to do this.

By cooling the system much below the tricritical temperature, a sudden significant jump in the coexistence curve (Fig. 12) occurs on the high-density side. Further analysis shows that the system crystallizes into a solid phase. Below the crystallization temperature, we find coexistence of a paramagnetic gas phase with a *square lattice* ferromagnetic solid phase, see Fig. 15(b). To distinguish the solid from the liquid phase, we performed Voronoi constructions of the configurations (shown to be a useful starting point to study the liquid-solid transition, e.g., by Fraser and co-workers[53]), which are plotted together with the corresponding particle positions and magnetic moments. For comparison, we also present in Fig. 15(a) a snapshot of a typical gas-liquid phase coexistence configuration including Voronoi tesselation.

Due to the particular choice of the magnetic interaction $J(r)$ of square well type in conjunction with the hard core repulsion, the square lattice structure is favored[51] at low temperatures relative to the hexagonal structure, which is the stable solid phase of the unperturbed hard disk system. Since we find apparently *coexistence* of a liquid phase and square lattice solid at $(T^*, \bar{\rho}^*) = (0.2, 0.8)$, but no longer at (0.3, 0.8), see, e.g., Figs. 15(d) and 15(c), and in conjunction with the jump in density in Fig. 12, we have a a strong hint for a first-order gas-square solid transition in our model, resulting in a *triple* point; recent overviews on 2D melting can be found in Refs. 3 and 4. We are able to locate the corresponding triple point temperature by the very sudden jump in the densities of the condensed phases at $T^*_{\text{triple}} = 0.16 \pm 0.01$. Thus the block analysis method is useful not only to determine the gas-liquid coexistence line, but also gas-solid transition densi-

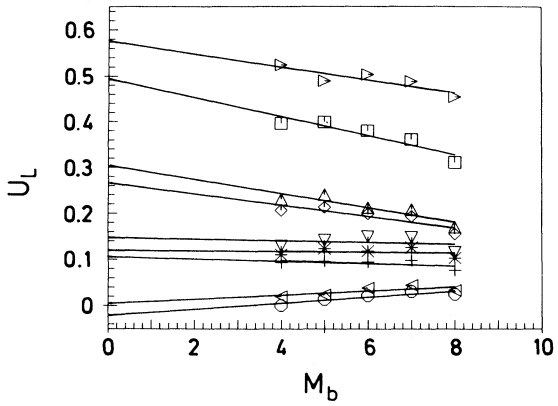

FIG. 14. Flow diagram of the cumulants U_L at the tricritical density as a function of the subsystem size M_b for different temperatures $T^* = \{0.3$, right-triangles; 0.4, squares; 0.5, up-triangles; 0.52, diamonds; 0.55, down-triangles; 0.57, stars; 0.6, crosses; 0.8, left-triangles; 1.0, circles$\}$. ($\bar{\rho}^* = 0.45$, $\omega_0/J = 4$, $J = 1$, $N = 200$, $T^*P \approx 40$.) The full lines are linear fits.

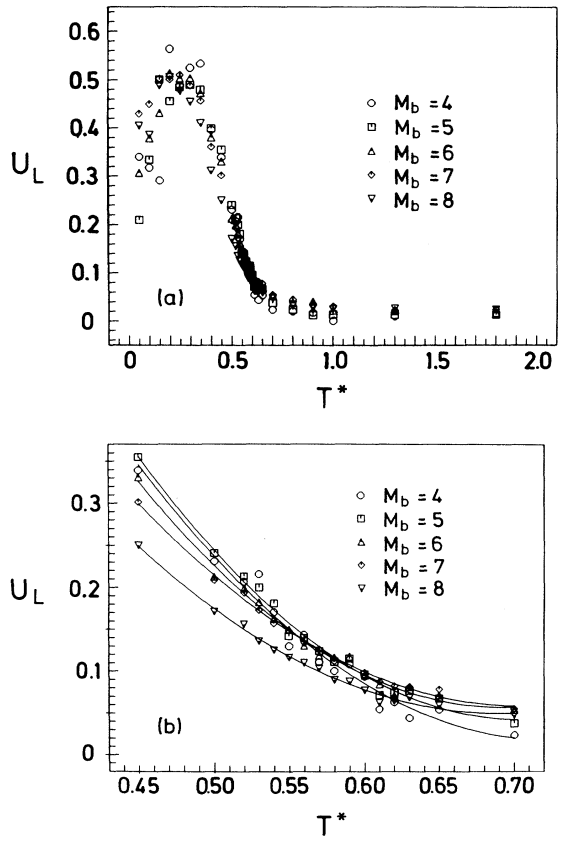

FIG. 13. Cumulants U_L at the tricritical density as a function of T^* for different blockings M_b as given in the insertion ($\bar{\rho}^* = 0.45$, $\omega_0/J = 4$, $J = 1$, $N = 200$, $T^*P \approx 40$). (a) Complete temperature range. (b) Blowup of (a) with full lines fitted through the data. Error bars are smaller than the size of the symbols.

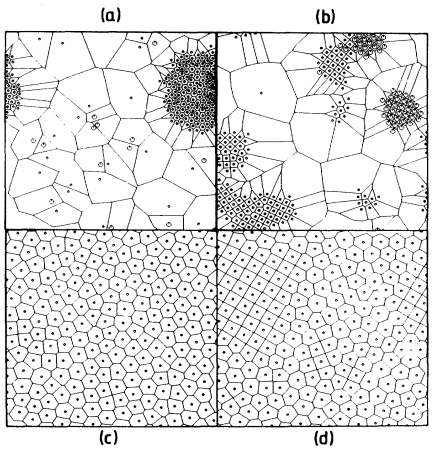

FIG. 15. Snapshot pictures of typical configurations with Voronoi constructions. (a) Gas-liquid coexistence ($T^* = 0.2$, $\bar{\rho}^* = 0.1$). (b) Gas-square solid coexistence ($T^* = 0.1$, $\bar{\rho}^* = 0.2$). (c) Liquid phase ($T^* = 0.3$, $\bar{\rho}^* = 0.8$). (d) Liquid phase-square solid coexistence ($T^* = 0.2$, $\bar{\rho}^* = 0.8$). The average magnetic moments of the particles, see text, are indicated by large (up) and small (down) circles.

ties including triple points, without having the problem of possibly biasing the lattice structure by the boundary conditions. Note that in the Gibbs ensemble[24,25] the study of coexistences including solid phases is hampered by the particle insertion problem.[54]

The order parameter Φ as defined in (8) is shown as a function of the temperature in Fig. 16. The circles are data points where both coexisting densities are available. For the few data marked with diamonds, no gas density was determined at the corresponding temperature, and we just interpolated linearly between the neighboring gas densities; a quick inspection of the phase diagram in Fig. 12 justifies this treatment in the respective temperature range. In the same figure, we indicate with a dashed (dotted) line the tricritical (triple) temperature as already determined. One can see the *continuously vanishing* order parameter clearly upon approaching the tricritical temperature from below, as well as the *jump* in Φ at the triple temperature. Above $T^* = 0.56$ we could no longer resolve any density differences.

As presented in Sec. III A, the density cumulants can also be used to locate the triple point. Inspection of our data clearly shows the statistics far from being sufficient for this purpose; and disorder averages over many realizations of the partly frozen system are probably necessary. However, the general trend is verified by the simulation. These observations may be useful in simulations of phase transitions of adsorbates involving coexistence of registered and nonregistered phases with different densities. In our 2D phase diagram we have an additional problem in that the coexistence curve is rather flat due to the exponent of the order parameter. This leads to a narrow region in the $U_L(T^*, \bar{\rho}^*_{\rm tri})$ diagram Fig. 13, where the cumulants have to decay from a maximum value and then even change the sign of their curvature around the triple temperature. The Lennard-Jones fluid in 3D has a much larger temperature range[55,21] where gas and liquid coexist, as compared to the same model in 2D; and the cumulant method approach to the gas-solid coexistence line and the triple point could be useful for *directly* estimating these quantities from simulation.

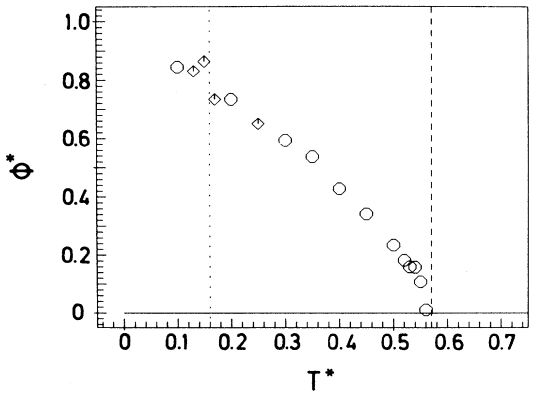

FIG. 16. Order parameter $\Phi^* = \Phi R^2$ as a function of T^*. ($N = 200$, $\omega_0/J = 4$, $J = 1$, $T^*P \approx 40$.) Dashed line, tricritical temperature; dotted line, triple temperature; circles are obtained using directly the definition of Φ, diamonds as discussed in the text. No error bars are shown.

A very recent density functional calculation of freezing in our system[51] supports the occurrence of a *thermodynamically stable* square lattice solid phase at low temperatures, and the corresponding triple temperature of $T^*_{\rm triple} \approx 0.1$ is in reasonable agreement with the PIMC simulation; please note that this density functional approach is based on a perturbation expansion for the solid phase starting from the liquid. This supports our conclusion that we observe no artifact of the simulation or metastable states.[50] However, the density functional theory predicts (using values for the parameters as in the PIMC simulation) a gas-*hexagonal* solid transition in between the gas-liquid and gas-*square* solid transitions, and thus two triple points associated with each of these coexistences. Since the MF tricritical temperature is off by a factor of 2, but is very sensitive to the actual value of the quantum parameter ω_0/J, see Fig. 4, one can squeeze the gas-hexagonal solid phase to lower temperatures by choosing an effective quantum parameter, which at the same time brings the MF tricritical point into better agreement with the PIMC data. On the other hand, we cannot strictly rule out the possibility that we also actually have a gas-hexagonal solid coexistence in the simulation, which was simply not monitored. Since a careful examination of this point is very intricate, we must leave this question open for the time being and leave it for future study.

V. SUMMARY, CONCLUSIONS, AND OUTLOOK

The present investigation shows that ideas familiar from the computer simulation study of phase transitions and critical phenomena, such as subblock analysis and the finite-size scaling recently generalized from classical lattice models to fluids,[36,37] can be carried over to fluids with internal quantum states as well. Using a simple model for molecules adsorbed on a substrate, we have demonstrated that such a program can indeed be carried out explicitly. In many respects, this study cannot be as sophisticated as that of the classical fluids, which in turn is already considerably more demanding in computational resources and data analysis than the lattice gas case. We do feel, however, that the methods developed in the present paper are a useful approach with which to study phase coexistence in fluids and adsorbates, including the vicinity of the critical point. As in the case of the lattice gas model, rather small subsystems of medium-size total systems can yield good estimates of the densities of coexisting phases. Note that a single, but statistically strong, simulation run yields information on both coexisting phases, simultaneously on many subsystem sizes and already allows some estimation of finite-size effects. Without these features, it would be out of range to map a phase diagram as the one presented here with such an accuracy. A meaningful study of properties such as critical exponents and amplitudes still seems to be out of range, at least for fluids with quantum degrees of freedom.

More precisely, in the present investigation we mapped

with satisfactory accuracy the phase diagram of a two-dimensional hard core fluid with internal quantum states represented as interacting two-level systems. To do so, we used a combination of path-integral Monte Carlo simulations and finite-size block analysis techniques. We can supply reliable estimates for central quantities of interest such as the tricritical and triple point and the binodal line of the coexisting phases. This allows one to determine shifts of the phase boundaries due to quantum fluctuations and thus to quantify the influence of quantum effects for a particular model system. The compressibilities extrapolated to the infinite system can also be obtained, though larger systems than studied here are clearly required if the compressibilities of the coexisting phases are of interest. In addition to the interesting phase diagram and fluctuations, we found a *square* lattice solid phase in *coexistence* with a gas phase at low temperatures. We also discussed an extension of the density block analysis method, which up to now has been used to determine the gas-liquid properties, to the location of gas-solid coexistence densities and thus triple points.

The issue raised by the occurrence of the gas-*hexagonal* solid coexistence remains open at the moment, and appropriately defined order parameters (e.g., monitoring bond orientational order[56] or Voronoi constructions[53]) to distinguish the different solid phases have to be evaluated. Still more challenging and at the same time more realistic would be to look carefully at this special point with an underlying corrugation potential modeling the substrate. This would also allow one to study commensurate-incommensurate competitive effects in conjunction with the influence of the internal quantum structure. We feel that such a very interesting investigation should be done in a different ensemble than the canonical one, and can be done only if considerable computational resources are supplied. As a next step in our aim to understand better the phase transitions of 2D adsorbed layers with internal quantum states, we plan to study the present or a similar Hamiltonian in the Gibbs ensemble.[57] In addition, we follow another route to incorporate continuous internal quantum degrees of freedom such as rotations[58,59] instead of the two-level approximation and to use more realistic potentials. It is hoped that the resulting Hamiltonians can be studied with similar techniques like the ones developed in the present paper, allowing one to quantitatively determine the quantum shifts of phase transitions. In view of the large deviations of the mean-field results from simulation in two dimensions, we feel that the techniques presented here will have a widespread application also in the investigation of cooperative phenomena in more general adsorbate models.

ACKNOWLEDGMENTS

It is a pleasure for us to thank Surajit Sengupta for fruitful discussions. The support (Bi 314/5) from the Deutsche Forschungsgemeinschaft is gratefully acknowledged by D. M. as well as grants of computer time on the Cray-YMP (HLRZ Jülich) and VP 100 (RHRK Kaiserslautern) vector processors. P. N. thanks the DFG for financial support.

[1] *Ordering in Two Dimensions,* edited by S. K. Sinha (North-Holland, Amsterdam, 1980).

[2] *Phase Transitions and Critical Phenomena,* edited by C. Domb and J. L. Lebowitz (Academic, London, 1987), Vol. 11.

[3] K. J. Strandberg, Rev. Mod. Phys. **60**, 161 (1988).

[4] H. Kleinert, *Gauge Fields in Condensed Matter* (World Scientific, Singapore, 1989), Vol. II, Part III, Chap. 14.

[5] *Phase Transitions in Surface Films 2,* edited by H. Taub, G. Torzo, H. J. Lauter, and S. C. Fain, Jr. (Plenum, New York, 1991); *Excitations in 2D and 3D Quantum Fluids,* edited by A. F. G. Wyatt and H. J. Lauter (Plenum, New York, 1991).

[6] H. Wiechert, Physica B **169**, 144 (1991).

[7] J. M. Gottlieb and L. W. Bruch, Phys. Rev. B **40**, 148 (1989); **41**, 7195 (1990).

[8] A. D. Novaco, Phys. Rev. Lett. **60**, 2058 (1988); A. D. Novaco and J. P. Wroblewski, Phys. Rev. B **39**, 11364 (1989).

[9] F. F. Abraham and J. Q. Broughton, Phys. Rev. Lett. **59**, 64 (1987); J. Q. Broughton and F. F. Abraham, J. Phys. Chem. **92**, 3274 (1988); F. F. Abraham, J. Q. Broughton, P. W. Leung, and V. Elser, Europhys. Lett. **12**, 107 (1990).

[10] P. R. Kubik and W. N. Hardy, Phys. Rev. Lett. **41**, 257 (1978); P. R. Kubik, W. N. Hardy, and J. Glattli, Can. J. Phys. **63**, 605 (1985).

[11] A. B. Harris and A. J. Berlinsky, Can. J. Phys. **57**, 1852 (1979).

[12] D. D. Awschalom, G. N. Lewis, and S. Georgy, Phys. Rev. Lett. **51**, 586 (1983); R. Marx and B. Christoffer, *ibid.* **51**, 790 (1983); J. Stoltenberg and O. E. Vilches, Phys. Rev. B **22**, 2920 (1980).

[13] R. Marx and B. Christoffer, Phys. Rev. B **37**, 9518 (1988).

[14] P. Nielaba, J. L. Lebowitz, H. Spohn, and J. L. Vallés, J. Stat. Phys. **55**, 745 (1989).

[15] D. Chandler and L. R. Pratt, J. Chem. Phys. **65**, 2925 (1976); K. S. Schweizer, R. M. Stratt, D. Chandler, and P. G. Wolynes, *ibid.* **75**, 1347 (1981); D. Chandler, K. S. Schweizer, and P. G. Wolynes, Phys. Rev. Lett. **49**, 1100 (1982).

[16] J. S. Hoye and G. Stell, Phys. Rev. Lett. **36**, 1569 (1976); J. Chem. Phys. **75**, 5133 (1981); E. Martina and G. Stell, J. Stat. Phys. **27**, 407 (1982).

[17] R. W. Hall and P. G. Wolynes, J. Stat. Phys. **43**, 935 (1986); Phys. Rev. B **33**, 7879 (1986).

[18] R. M. Stratt, J. Chem. Phys. **80**, 5764 (1984); Phys. Rev. Lett. **53**, 1305 (1984); S. G. Desjardins and R. M. Stratt, J. Chem. Phys. **81**, 6232 (1984).

[19] P. Ballone, Ph. de Smedt, J. L. Lebowitz, J. Talbot, and E. Waisman, Phys. Rev. A **35**, 942 (1987); Ph. de Smedt, P. Nielaba, J. L. Lebowitz, J. Talbot, and L. Dooms, *ibid.* **38**, 1381 (1988).

[20] A. Amann, in *Large Scale Molecular Systems: Quantum and Stochastic Aspects—Beyond the Simple Molecular Picture,* edited by W. Gans, A. Blumen, and A. Amann (Plenum, New York, 1991).

[21] D. Levesque and J. J. Weis, in *Monte Carlo Methods in*

Condensed Matter Physics, edited by K. Binder (Springer, Berlin, 1992).
[22]K. Binder and D. P. Landau, in *Advances in Chemical Physics* **LXI**, edited by K. P. Lawley (Wiley, New York, 1989).
[23]K. Binder, Rep. Prog. Phys. **50**, 783 (1987).
[24]A. Z. Panagiatopoulos, Mol. Phys. **61**, 813 (1987); A. Z. Panagiatopoulos, N. Quirke, M. Stapleton, and D. Tildesley, *ibid.* **63**, 527 (1988); A. Z. Panagiatopoulos, Mol. Sim. **9**, 1 (1992).
[25]B. Smit, Ph. de Smedt, and D. Frenkel, Mol. Phys. **68**, 931 (1989); B. Smit and D. Frenkel, J. Chem. Phys. **94**, 5663 (1991); B. Smit, *Simulation of Phase Coexistence: From Atoms to Surfactants* (Proefschrift, Rijksuniversiteit Utrecht, 1990).
[26]A. D. Bruce and N. B. Wilding, Phys. Rev. Lett. **68**, 193 (1992); N. B. Wilding and A. D. Bruce, J. Phys. Condens. Matter **4**, 3087 (1992).
[27]D. Marx, P. Nielaba, and K. Binder, Phys. Rev. Lett. **67**, 3124 (1991); D. Marx, Surf. Sci. **272**, 198 (1992).
[28]L. W. Bruch, Surf. Sci. **125**, 194 (1983).
[29]J. A. Barker, J. Chem. Phys. **70**, 2914 (1979); D. Chandler and P. G. Wolynes, *ibid.* **74**, 4078 (1981).
[30]*Monte Carlo Methods in Quantum Problems,* edited by M. H. Kalos (Plenum, New York, 1982).
[31]B. J. Berne and D. Thirumalai, Annu. Rev. Phys. Chem. **37**, 401 (1986).
[32]*Quantum Monte Carlo Methods,* edited by M. Suzuki (Springer, Berlin, 1987).
[33]*Quantum Simulations of Condensed Matter Phenomena,* edited by J. D. Doll and J. E. Gubernatis (World Scientific, Singapore, 1990).
[34]D. Chandler, in *Liquids, Freezing and Glass Transition,* edited by J. P. Hansen, D. Levesque, and J. Zinn-Justin (Elsevier, Amsterdam, 1991).
[35]K. E. Schmidt and D. M. Ceperley, in *Monte Carlo Methods in Condensed Matter Physics*, edited by K. Binder (Springer, Berlin, 1992).
[36]M. Rovere, D. W. Heermann, and K. Binder, Europhys. Lett. **6**, 585 (1988); J. Phys. Condens. Matter **2**, 7009 (1990).
[37]M. Rovere, P. Nielaba, and K. Binder, Z. Phys. B (to be published).
[38]*Finite Size Scaling and Numerical Simulation*, edited by V. Privman (World Scientific, Singapore, 1990).
[39]K. Binder, Z. Phys. B **43**, 119 (1981); Phys. Rev. Lett. **47**, 693 (1981).
[40]K. Binder, Ferroelectrics **73**, 43 (1987).
[41]M. N. Barber, in *Phase Transitions and Critical Phenomena*, edited by C. Domb and J. L. Lebowitz (Academic, London, 1983), Vol. 8.
[42]*Monte Carlo Methods in Statistical Physics*, edited by K. Binder (Springer, Berlin, 1979); *Applications of the Monte Carlo Methods in Statistical Physics*, edited by K. Binder (Springer, Berlin, 1984); *Monte Carlo Methods in Condensed Matter Physics*, edited by K. Binder (Springer, Berlin, 1992).
[43]K. Binder and D. W. Heermann, *Monte Carlo Simulation in Statistical Physics–An Introduction* (Springer, Berlin, 1988).
[44]M. Suzuki, Prog. Theor. Phys. **46**, 1337 (1971); **56**, 1454 (1976); Commun. Math. Phys. **51**, 183 (1976).
[45]M. F. Herman, E. J. Bruskin, and B. J. Berne, J. Chem. Phys. **76**, 5150 (1982); J. Cao and B. J. Berne, *ibid.* **91**, 6359 (1989).
[46]D. Marx, P. Nielaba, and K. Binder, Int. J. Mod. Phys. C **3**, 337 (1992).
[47]R. M. Fye, Phys. Rev. B **33**, 6271 (1986); J. Stat. Phys. **43**, 827 (1986); R. M. Fye and R. T. Scalettar, Phys. Rev. B **36**, 3833 (1987).
[48]E. L. Pollock and D. M. Ceperley, Phys. Rev. B **30**, 2555 (1984).
[49]F. Lado, J. Chem. Phys. **49**, 3092 (1968).
[50]K. Binder, in *Material Sciences and Technology*, edited by P. Haasen (Verlag Chemie, Weinheim, 1991), Vol. 5.
[51]S. Sengupta, D. Marx, and P. Nielaba, Europhys. Lett. **20**, 383 (1992).
[52]I. D. Lawrie and S. Sarbach, in *Phase Transitions and Critical Phenomena*, edited by C. Domb and J. L. Lebowitz (Academic, London, 1984), Vol. 9.
[53]D. P. Fraser, M. J. Zuckermann, and O. G. Mouritsen, Phys. Rev. A **42**, 3186 (1990).
[54]M. Stapleton (private communication).
[55]D. Levesque, J. J. Weis, and J. P. Hansen, in *Monte Carlo Methods in Statistical Physics*, edited by K. Binder (Springer, Berlin, 1979); D. Levesque, J. J. Weis, and J. P. Hansen, in *Applications of the Monte Carlo Methods in Statistical Physics*, edited by K. Binder (Springer, Berlin, 1984).
[56]P. J. Steinhardt, D. R. Nelson, and M. Ronchetti, Phys. Rev. B **28**, 784 (1983); Z. Q. Wang and D. Stroud, J. Chem. Phys. **94**, 3896 (1991).
[57]F. Schneider (unpublished).
[58]D. Marx and P. Nielaba, Phys. Rev. A **45**, 8968 (1992); D. Marx (unpublished).
[59]D. Marx, O. Opitz, P. Nielaba, and K. Binder (unpublished).